

Article

# Graphene Oxide from Graphite of Spent Batteries as Support of Nanocatalysts for Fuel Hydrogen Production

Gabriel Sperandio , Iterlandes Machado Junior , Esteffany Bernardo and Renata Moreira \*

Department of Chemistry, Campus Universitário, Universidade Federal de Viçosa, Av. Peter Henry Holfs, s/n, Viçosa 36570-900, Brazil; gabriel.sperandio@ufv.br (G.S.); iterlandes.junior@ufv.br (I.M.J.); esteffany.bernardo@ufv.br (E.B.)

\* Correspondence: renata.plopes@ufv.br; Tel.: +55-31-3612-6676

**Abstract:** The increasing production of electronic waste and the rising demand for renewable energy are currently subjects of debate. Sustainable processes based on a circular economy are required. Then, electronic devices could be the main source for the synthesis of new materials. Thus, this work aimed to synthesize graphene oxide (GO) from graphite rod of spent Zn-C batteries. This was used as support for Ni/Co bimetallic nanocatalysts in the evolution of hydrogen from  $\text{NaBH}_4$  for the first time. The graphene oxide (GO) exhibited a diffraction peak at  $2\theta = 9.1^\circ$ , as observed using X-ray diffraction (XRD), along with the presence of oxygenated groups as identified using FTIR. Characteristic bands at  $1345$  and  $1574 \text{ cm}^{-1}$  were observed using Raman spectroscopy. A leaf-shaped morphology was observed using SEM. GO sheets was observed using TEM, with an interplanar distance of  $0.680 \text{ nm}$ . Ni/Co nanoparticles, with an approximate size of  $2 \text{ nm}$ , were observed after deposition on GO. The material was used in the evolution of hydrogen from  $\text{NaBH}_4$ , obtaining an efficiency close to  $90\%$ , with a kinetic constant of  $0.0230 \text{ s}^{-1}$  at  $296.15 \text{ K}$  and activation energy of  $46.7 \text{ kJ mol}^{-1}$ . The material showed an efficiency in seven reuse cycles. Therefore, a route of a new material with added value from electronic waste was obtained from an eco-friendly process, which can be used in  $\text{NaBH}_4$  hydrolysis.

**Keywords:** e-waste; metallic nanoparticles; catalysis; eco-friendly process; sustainability



**Citation:** Sperandio, G.; Junior, I.M.; Bernardo, E.; Moreira, R. Graphene Oxide from Graphite of Spent Batteries as Support of Nanocatalysts for Fuel Hydrogen Production. *Processes* **2023**, *11*, 3250. <https://doi.org/10.3390/pr11113250>

Academic Editors: Dimitris Zagklis and Georgios Bampos

Received: 24 October 2023

Revised: 8 November 2023

Accepted: 16 November 2023

Published: 19 November 2023



**Copyright:** © 2023 by the authors. Licensee MDPI, Basel, Switzerland. This article is an open access article distributed under the terms and conditions of the Creative Commons Attribution (CC BY) license (<https://creativecommons.org/licenses/by/4.0/>).

## 1. Introduction

Demand for portable electrical energy storage devices has increased in recent years due to rapid technological advances and the lifestyle adopted by society. This phenomenon has led to an increase in the disposal of obsolete equipment, which is denominated e-waste [1]. According to the report of the International Renewable Energy Agency, in 2023, batteries will be responsible for the storage of  $14,000 \text{ MW}$  of charge, with an annual revenue of  $\text{USD } 18 \text{ billion}$  [2].

Among the different types of batteries, Zn-C cells have a cathode made of graphite carbon, which can be used as a precursor for graphene oxide (GO). Among various types of batteries, Zn-C cells feature a cathode constructed from graphite carbon, which can serve as a precursor for graphene oxide (GO). Moreover, within this type of battery, zinc cups are still available for metal recycling [3], and the electrolytic paste contains zinc manganese dispersed in graphite powder, which has demonstrated utility as a photocatalytic to various catalytic reactions [4].

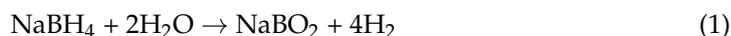
Graphene oxide is a material that precedes graphene or reduced graphene oxide (GO-r) in graphite chemical exfoliation processes. This material is obtained from graphite through an oxidation reaction, leading to the formation of surface oxygenated groups, including carbonyls, carboxyls, and epoxy groups. This creates a carbon-rich structure with  $\text{sp}^3$  hybridization. Despite the structural differences, which lead to specific chemical behavior, GO has thermal, optical and mechanical properties similar to graphene [5]. Graphene oxide

has been obtained using different raw materials, from graphite to pomelo peels [6]. This combination of characteristics makes this material highly appealing for a wide range of applications, paving the way for exploring new methods of synthesis [7].

There are different chemical exfoliation processes for graphite to obtain GO such as the Staudenmaier method [8], the Hoffman method [9] and the Hummers method [10]. In general, such processes differ from each other according to the type of oxidizing agent used, as well as different concentrations of reagents [11]. The Staudenmaier method uses fuming nitric acid, concentrated sulfuric acid and potassium chlorate to promote the oxidation of graphite. For the method proposed by Hoffman, the fuming nitric acid is replaced by concentrated nitric acid [9]. For the Hummers method, concentrated sulfuric acid, sodium nitrate and potassium permanganate are used [10]. In all three cases, the product obtained is always the same, with subtle structural differences that do not affect its properties. The Hummers method has variations in the literature that make it more environmentally friendly. Among these modifications, Loudiki et al. performed the ultrasound-assisted oxidation of graphite [12]. According to the authors, the amount of reagent used is smaller compared to the original method, reducing production costs, generating less waste, and making the method eco-friendly. Furthermore, the material presented better characteristics, as its performance was evaluated using voltametric techniques.

Graphene oxide can be used for different purposes [13]. An interesting application consists in its use as a support for metallic nanoparticles [14]. The advantage of the support is to minimize the agglomeration of these materials at a nanometer scale, improving the efficiency of the nanocatalysts [15]. In addition, they configure a heterogeneous system, allowing their reuse in other catalytic cycles, in addition to preventing their leaching. Grad et al. used GO as a nanoparticle support for formic acid dehydrogenation [16]. Singla et al. used carbon-based nanomaterials, including GO, as photosensitizers in photocatalytic water separation reactions [17]. Another application that has shown to be very promising is its use in sodium borohydride decomposition reactions for the production of hydrogen [18].

Hydrogen gas is a strong candidate to replace fossil fuels due to its high specific heat of 28.851 J/(mol × K), in addition to generating water vapor as a combustion product [19]. However, its storage and transport cause serious risks because it is a flammable gas. Therefore, generating hydrogen in the place where it will be consumed is a highly promising alternative. This technology may be possible through the evolution of hydrogen from metal hydrides. These substances are solid at room temperature and have large amounts of hydrogen in their composition. Sodium borohydride, for example, contains 10.5% (*w/w*) of hydrogen, whose decomposition produces hydrogen gas (Equation (1)). Several catalysts can be used in the process, such as Co [18], Ni [20], Au [21] and Pt [16], among others.



The bimetallic composition, which involves more than one metal, has been highlighted due to the synergistic effect between the two metals. Among the bimetallic compositions, those of nickel and cobalt, which are anchored in different support materials, stand out. Sun et al. synthesized a Co-Ni bimetallic inlaid carbon sphere catalyst that showed promise in the evolution of hydrogen from NaBH<sub>4</sub> [22]. According to the authors, a hydrogen generation rate (HGR) of 6364 mL min<sup>-1</sup>g<sub>cat.</sub><sup>-1</sup> was obtained, with an efficiency of 83.4% after five cycles of use. Chou et al. produced a bimetallic catalyst of Ni and Co anchored in reduced graphene oxide that presented a hydrogen generation rate of 1280 mL min<sup>-1</sup>g<sub>cat.</sub><sup>-1</sup>, with an activation energy of 55.12 kJ mol<sup>-1</sup> [23]. A three-dimensional graphene network-supported nickel-cobalt bimetallic alloy nanocatalyst was prepared by Karaman [24]. This catalyst showed a hydrogen production rate of 82.65 mL min<sup>-1</sup>g<sub>cat.</sub><sup>-1</sup>, with an efficiency of 95.96% after five cycles of use [25]. Didehban et al. anchored nickel and cobalt bimetallic nanoparticles on magnetic zeolite and bentonite to produce a catalyst for the borohydride hydrolysis reaction [25]. The catalyst anchored in magnetic bentonite showed a hydrogen evolution rate of 186 mL min<sup>-1</sup>g<sub>cat.</sub><sup>-1</sup>. According to the authors, activation energies of 37.62 and 44.98 kJ mol<sup>-1</sup> were obtained for nanoparticles anchored in magnetic zeolite and

bentonite, respectively. Yue et al. produced nickel and cobalt microfibers decorated with Pd nanocatalysts for the evolution of hydrogen from  $\text{NaBH}_4$  [26]. According to the authors, a hydrogen evolution rate of  $680 \text{ mL min}^{-1} \text{ g}_{\text{cat}}^{-1}$  was obtained, maintaining 90% of its catalytic activity after 10 cycles.

In view of the above, this work aims to synthesize GO from spent Zn-C batteries as a support of metallic nanoparticles (Co and Ni) for the first time for use in borohydride hydrolysis catalysis to produce hydrogen gas. Although other components of the Zn-C cell can be recovered for diverse applications, the aim of this study was solely to enhance the value of the graphite component.

## 2. Materials and Methods

### 2.1. Standards and Reagents

Analytical-grade reagents were used in this work. Sodium nitrate 99% (CAS 7631-99-4) and sulfuric acid 97% (CAS 7664-93-9) were purchased from NEON (Suzano/São Paulo–Brazil). Potassium permanganate 99% (CAS 7722-64-7), hydrogen peroxide 30% (CAS 7722-84-1), sodium borohydride 98% (CAS 16940-66-2), nickel sulfate heptahydrate 98% (CAS 10101-97-0) and cobalt nitrate hexahydrate 98% (CAS 10026-22-9) were purchased from VETEC (Duque de Caxias/Rio de Janeiro–Brazil). Hydrochloric acid 37% (CAS 7647-01-0) was obtained from ALPHATEC (São Bernardo do Campo/São Paulo–Brazil). Graphite (CAS 7782-42-5) was purchased from ACS Científica (Sumaré/São Paulo–Brazil). All solutions were prepared using type 1 water, obtained with the Milli-Q system (Millipore Corporation, São Paulo/São Paulo–Brazil), and were always freshly prepared.

### 2.2. Obtaining and Processing of Raw Material

Zn-C batteries were purchased at a used battery collection center in the city of Viçosa, Minas Gerais, Brazil. Seven Zn-C batteries were opened with pliers to break the external zinc cup. The rod-shaped carbon cathode was removed with pliers and crushed to obtain a fine powder. Then, the material was sieved through an 80-mesh screen.

### 2.3. Synthesis of Graphene Oxide

The graphene oxide was synthesized according to the adapted Hummers method [10]. Then, 1000 g of processed graphite from spent Zn-C batteries, 1000 g of sodium nitrate and 50.00 mL of concentrated sulfuric acid were added to a round-bottomed flask. The system was affixed on an ultrasound device (frequency 40 kHz) containing an ice bath in its vat, for temperature control at  $0^\circ\text{C}$ . The system was kept in an exhaust hood for 15 min. A dark green color was observed. Subsequently, 6000 g of potassium permanganate was added slowly to the system at  $0^\circ\text{C}$  under sonication. A violet coloration was observed due to the presence of manganese (+7). The system was maintained under sonication at  $0^\circ\text{C}$  for another hour. Then, the color of the system changed from violet to brown, due to the change in the oxidation state of manganese. After this time, 100 mL of type 1 water was slowly added to the system, and the color changed to a dark brown. The system was sonicated for another two hours, and its temperature was controlled to not exceed  $80^\circ\text{C}$ . Then, another 400 mL of type 1 water was added, followed by the addition of 12 mL of hydrogen peroxide (30%). This step was necessary to eliminate the permanganate residues. Then, the system was centrifuged at 6000 rpm for 7 min, followed by three wash steps with hydrochloric acid 3% *v/v* solution. The solid GO was dried in an oven at  $35^\circ\text{C}$  for 12 h and stored at room temperature ( $25^\circ\text{C}$ ). For the sake of comparison, an identical synthesis was performed using analytical-grade graphite.

### 2.4. Synthesis of Metallic Nanoparticles Decorated on GO (NPs-M/GO)

For the NPs-M/GO synthesis, where *M* is the metal decorated on GO, 100 mg of GO was dispersed in 10 mL of type 1 water in a beaker. Subsequently, a certain amount of the metal precursor salt,  $\text{NiSO}_4 \cdot 7\text{H}_2\text{O}$  and/or  $\text{Co}(\text{NO}_3)_2 \cdot 7\text{H}_2\text{O}$ , according to Table 1, were added to the system, which remained under stirring for 15 min at room temperature

(25 °C). Then, 1.00 mL of a solution of NaBH<sub>4</sub> (1.00 mol L<sup>-1</sup>) was added to the system, which remained under stirring for another 15 min. The system was centrifuged at 6000 rpm for 7 min and washed three times with type 1 water. The freshly prepared material was used in the hydrogen evolution. Six different compositions of GO-decorated nanoparticles were prepared, as described in Table 1.

**Table 1.** Composition of nanoparticles decorated in graphene oxide.

System	Composition
NiNPs-GO	NiNPs
Co/Ni-NPs-GO (20:80 <i>w/w</i> )	Co/Ni ratio 20:80 <i>w/w</i>
Co/Ni-NPs-GO (40:60 <i>w/w</i> )	Co/Ni ratio 40:60 <i>w/w</i>
Co/Ni-NPs-GO (60:40 <i>w/w</i> )	Co/Ni ratio 60:40 <i>w/w</i>
Co/Ni-NPs-GO (80:20 <i>w/w</i> )	Co/Ni ratio 80:20 <i>w/w</i>
CoNPs-GO	CoNPs

### 2.5. Characterization of Materials

The materials were characterized using different techniques. X-Ray diffraction was performed with a Bruker D8-Discovery diffractor (Billerica, MA, USA), using copper metal as a target, working with a wavelength of 1.54 Å and horn of 45 kV. The sweep speed was 0.05° 2.5 s<sup>-1</sup> in a range of 5° to 40°. The materials were also characterized using Raman spectroscopy, using a MicroRaman—InVia Renishaw equipment (Kansai, Japan). A laser with a wavelength of 633 nm and power of 3 mW was used, with a number of co-additions equal to 5 and an integration time of 30 s. Thermogravimetric analysis was carried out using a NETZSCH (Selb, Germany), STA 449, with a reading range of 25 to 900 °C, with a variation of 10 °C min<sup>-1</sup>, in a synthetic air atmosphere. The size of the metallic nanoparticles was evaluated and characterized using Transmission Electron Microscopy (TEM) with the equipment Tecnai, G2-20 Supertwin FEI–200 kV (Hillsboro, OR, USA). The particle size and interplanar distance were determined using ImageJ software (Version: 1.8.0). The morphology was evaluated using Scanning Electron Microscopy (SEM) in a FEI Quanta and model 200 FEG device coupled with an X-ray energy dispersive detector. The functional groups present in the material were evaluated with Fourier Transform Infrared Spectroscopy. A VARIAN 660-IR instrument (Palo Alto, CA, USA) with a PIKE GladiATR attenuated total reflectance accessory with diamond crystal was used. The measure was evaluated in the wave number range from 200 to 4000 cm<sup>-1</sup>. An analysis of the surface area of the material as well as its element was performed using Scanning Electron Microscopy (SEM) and an Energy-Dispersive X-ray Spectrometer (EDS). The equipment used was a JEOL Scanning Electron Microscope (Kyoto, Japan), model JSM-6010LA, with a resolution of 4 nm and 20 kV, with application from 8 times to 300,000 times, accelerated voltage from 500 V to 20 kV, and an electron gun with formed tungsten filament pre-centered. An Everhart–Thornley detector for secondary electron imaging and a solid state detector for backscattered electrons with topography contrast, composition and variable shading were used. A silicon drift detector was used for EDS analysis with 133 eV resolution. The samples were also subjected to nitrogen adsorption measurement at –196 °C using a Nova Station A surface area analyzer from Quantachrome Instruments (Boynton Beach, FL, USA). Before conducting the measurements, the sample underwent a vacuum drying process at 100 °C for 4 h to eliminate any remaining water and gases. The specific surface area of the sample was then calculated using the BET method.

### 2.6. Hydrogen Evolution from Borohydride

An image of the reactor used in the catalysis of hydrogen evolution from borohydride catalysis is shown in Figure S1. The conditions used in this work were made according to (Su et al., 2023 [27]). The freshly prepared NPs-M/GO were dispersed in 10.00 mL of type 1 water in a kitassate, which was sealed with a rubber septum. The system was stirred on a magnetic stirrer at controlled temperature. The system was connected through the

kitassato side outlet to the hydrogen gas collector by a rubber hose. Subsequently, 1.00 mL of sodium borohydride solution ( $0.500 \text{ mol L}^{-1}$ ) was introduced into the system with the aid of a syringe and the reaction time was timed.

### 2.7. Reaction Parameters Evaluation

Under the conditions mentioned above, assays were carried out to evaluate the influence of (1) different concentrations of  $\text{NaBH}_4$ , (2) different dose of the catalyst, (3) different concentrations of  $\text{NaOH}$ , (4) different temperatures, and (5) reuse of the material.

#### 2.7.1. Evaluation of the Influence of $\text{NaBH}_4$ Concentration

The hydrogen evolution was carried out using different  $\text{NaBH}_4$  concentrations, i.e., 0.200, 0.300, 0.400 and  $0.500 \text{ mol L}^{-1}$ . The amount of catalyst Ni/Co NPs (60:40 *w/w*) was fixed in 0.700 mmol anchored in 100 mg of GO support; volume of 1.00 mL  $\text{NaBH}_4$  solution (at the target concentration); temperature at 296.15 K.

#### 2.7.2. Evaluation of the Influence of Catalyst Dose

Hydrogen evolution was carried out using different Ni/Co NPs (60:40 *w/w*) doses, i.e., 0.175, 0.350, 0.525, 0.700 mmol. In these assays, other parameters were fixed, such as GO support mass (100 mg) and volume of 1.00 mL  $\text{NaBH}_4$  solution ( $0.500 \text{ mol L}^{-1}$ ).

#### 2.7.3. Temperature

Hydrogen evolution was carried out at different temperatures: 296.15; 304.15; 313.15 and 321.15 K. In these assays, the other parameters were fixed, such as 0.700 mmol of Ni/Co NPs (60:40 *w/w*), GO support mass (100 mg); volume of 1.00 mL  $\text{NaBH}_4$  solution ( $0.500 \text{ mol L}^{-1}$ ).

#### 2.7.4. NaOH Influence

Four sodium hydroxide solutions were prepared: 0.010, 0.050, 0.100,  $0.200 \text{ mol L}^{-1}$  in type 1 water. The nanoparticles were dispersed in 10.00 mL of each alkaline solution. In these assays, the other parameters were fixed, such as GO support mass (100 mg); 0.700 mmol of Ni/Co NPs (60:40 *w/w*); volume of 1.00 mL  $\text{NaBH}_4$  solution ( $0.500 \text{ mol L}^{-1}$ ); temperature at 296.15 K.

#### 2.7.5. Reuse of the Material

The reuse of Ni/Co-GO NPs was evaluated. For this, the above-mentioned initial conditions were used, setting the parameters as follows: mass of catalyst (100 mg); 0.700 mmol of Ni/Co NPs (60:40 *w/w*); 1.00 mL of  $\text{NaBH}_4$  solution ( $0.500 \text{ mol L}^{-1}$ ); temperature at 296.15 K. Following every cycle, the resulting suspension was washed with 30 mL of type 1 water, followed by centrifugation at 5000 rpm for 7 min to recover the solid material. The recovered solid was dispersed again in 10.00 mL of type 1 water and reintroduced into the kitassate for another cycle. This operation was carried out until the deactivation of the catalyst was observed.

#### 2.7.6. Activation Energy

Firstly, the kinetic constant of the reaction was determined according to Equation (2) for each temperature; the procedure is described in Section 2.7.3. The temperatures evaluated were 296.15; 304.15; 313.15 and 321.15 K.

$$k = -4d[\text{NaBH}_4]/t = d[\text{H}_2]/dt \quad (2)$$

The activation energy was calculated using the Arrhenius equation (Equation (3)).

$$\ln(k) = \ln(A) - \frac{Ea}{RT} \quad (3)$$

where  $k$  is the kinetic constant of the reaction,  $A$  is the pre-exponential factor,  $E_a$  is the apparent activation energy in kJ/mol,  $R$  is the universal gas constant and  $T$  is the absolute temperature.

### 3. Results and Discussion

#### 3.1. Material Characterization

The obtained graphene oxide from the graphite of spent batteries showed a 95% yield. The small loss of material can be attributed to stages of purification, i.e., washing and centrifugation steps. The GO presented a black color (Figure S2). Its appearance in powder form showed good separation between its grains, which provides good dispersion in water. Similar results were obtained by Loudiki et al. [12]. The SEM image of GO is shown in Figure 1. It can be seen that GO has a leaf-like morphology with different sizes and a highly porous structure. The material had a specific surface area of  $31.048 \text{ m}^2 \text{ g}^{-1}$ . Jia et al. [18] reached a value of  $89 \text{ m}^2 \text{ g}^{-1}$  for the formation of a GO-supported phosphorus/cobalt boride catalyst via in situ reduction. This catalyst was employed in the hydrolysis of  $\text{NaBH}_4$  to generate hydrogen gas. Liu et al. [20] found a specific surface area of  $1.98 \text{ m}^2 \text{ g}^{-1}$  and  $1.15 \text{ m}^2 \text{ g}^{-1}$  for Ni powder and Co powder, respectively. These materials were utilized in the hydrolysis reaction of borohydride for hydrogen production.

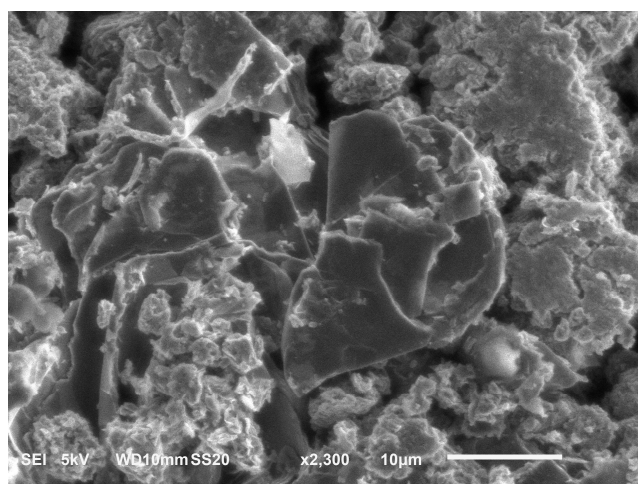


**Figure 1.** Scanning Electron Microscopy of graphene oxide obtained from spent Zn-C batteries synthesized using the adapted Hummers method.

XRD analysis was used to investigate the conversion of graphite from Zn-C batteries to GO. Figure 2a shows the graphite diffractogram from spent batteries. A sharp diffraction peak can be observed at  $2\theta = 26.4^\circ$ , which can be attributed to the basal plane (002) of the graphite, with a lamellar distance of  $3.37 \text{ \AA}$  [28]. Such results indicate a hexagonal crystal structure for the carbon atoms, characteristic of graphite. Additionally, wide diffraction peaks are also observed at  $42.5$  and  $55^\circ$ , which can be attributed to the (100) and (004) planes, respectively. On the other hand, GO presented a broad peak between  $15$  and  $30^\circ$ . More detailed information can be observed in Figure 2b, which indicates the formation of an amorphous structure. This occurs due to the oxidation of graphite and detachment of the carbon planes [12]. The peak at  $2\theta = 9.2^\circ$  is related to the emergence of interactions between the functional groups that are formed in the GO [19]. Based on the results, it can be concluded that GO was successfully synthesized. However, the presence of peaks attributed to graphite, at  $2\theta = 26.4^\circ$  and  $42.4^\circ$ , indicate a residual amount of graphite in the GO obtained. For Ni/Co-GO NPs, a more amorphous character after the deposition of the NPs was observed. According to Zhang et al., the diffraction peak at  $2\theta = 34^\circ$  can be attributed to the metal hydroxides formed during the deposition of nanoparticles [29]. The peaks of Ni and Co were not observed due to the low concentration of these metals in the material.

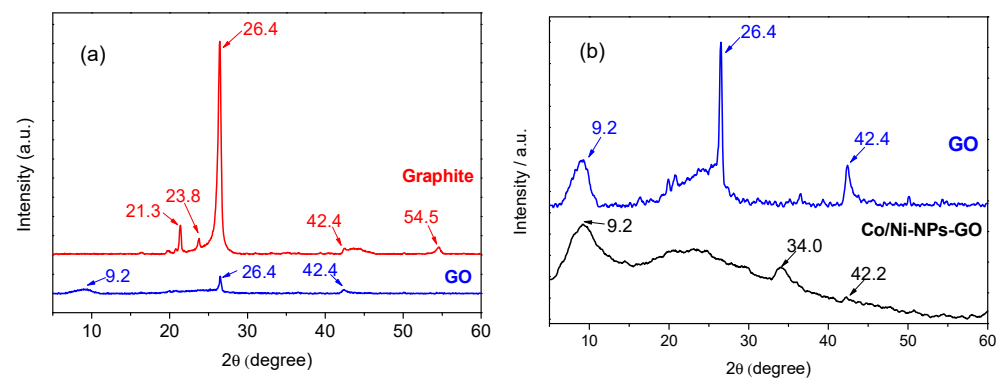


**Figure 2.** (a) Diffractogram of graphite and graphene oxide (GO) obtained from spent Zn-C batteries synthesized using the adapted Hummers method; (b) diffractogram of GO and Ni/Co-GO NPs (60:40 *w/w*).

The materials were also characterized using Transmission Electron Microscopy and the GO results can be seen in Figure 3. GO leaf-like morphology with different transparencies can be observed, corroborating the results obtained using SEM. Dark areas indicate stacking of several layers of GO, while areas of greater transparency indicate a thinner film of a few layers of GO. Similar results were observed by Stobinski et al. [30]. The electron diffraction rings obtained from Selected-Area Electron Diffraction (SAED) measurements (Figure S3) exhibited spacings of approximately 0.98 Å, 1.19 Å, 2.10 Å, and 3.00 Å. These findings are indicative of “*d*” spacings of graphene, signifying the existence of graphitic regions. Similar results were documented by Saxena et al. [31]. After the Ni/Co NPs deposition on GO, a modification of the diffraction pattern was observed, with “*d*” spacing of about 1.22 Å; 1.65 Å; 2.06 Å; 3.19 Å; and 3.80 Å (Figure S4). Therefore, it can be concluded that Ni/Co NPs deposition was successfully performed. The material presented an interplanar distance of 0.680 nm, as shown in Figure 3a. Similar results were found by Aliyev et al. [32], who found an interplanar distance of 0.65 nm between the GO layers. The Ni/Co NPs were evenly distributed over the material surface, with a size of 1.55 nm ± 0.05 (Figure 3b). Similar results were observed by Dong et al. [15], who obtained nanoparticles with sizes between 2.9 nm and 4.2 nm. The determined interplanar distance was 0.269 nm, which can be attributed to the presence of Ni/Co nanoparticles [33,34].

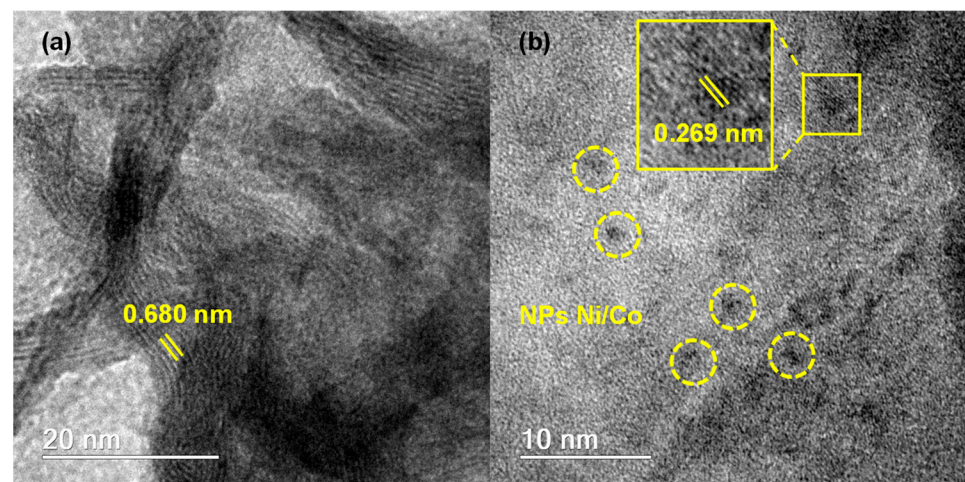


**Figure 3.** Transmission Electron Microscopy images of graphene oxide obtained from spent Zn-C batteries synthesized using the adapted Hummers method. (a) Interplanar distance between the GO planes (b) Ni/Co nanoparticles decorated on the GO.

The X-ray Energy Dispersive Spectroscopy results, extracted from the images displayed in Figures S3 and S4, are presented in Figure S5. The GO is composed of carbon (40.7%) and oxygen (12.7%). Other elements are also observed in smaller amounts, such as sodium, aluminum, silicon, sulfur, potassium, and manganese, which can be attributed to impurities arising from graphite or the reagents used in the synthesis. The presence of copper is due to the grid used in the analysis. After the deposition of the nanoparticles, the presence of Ni (9.8%) and Co (6%) elements can be observed, in addition to carbon (25.1%) and oxygen (12.5%).

The FTIR spectra of the materials obtained are shown in Figure S6. The results of graphite and GO are shown in Figure S6a. A main band at  $3435\text{ cm}^{-1}$  can be observed, which can be attributed to the stretching of hydroxyl groups ( $\nu\text{OH}$ ) bonds [35], due to the presence of water in the materials. After the graphite oxidation process to obtain GO, two bands are observed at  $1730\text{ cm}^{-1}$  and  $1630\text{ cm}^{-1}$ , which can be attributed to the stretching of carbonyl ( $\nu\text{C=O}$ ) of carboxylic acids, esters, and ketones [36]. The bands at  $1226\text{ cm}^{-1}$  and  $1051\text{ cm}^{-1}$ , also present in GO, can be attributed to the C–O stretching vibrations [28]. The presence of the carbonyl group formed in GO facilitates the fixation of metallic nanoparticles on the surface of the composite [36]. According to Naveen et al. [37], the band at  $1081\text{ cm}^{-1}$  can be attributed to stretching vibrations of epoxy (CO). The Ni/Co-GO NPs spectrum is shown in Figure S6b. Bands at  $520\text{ cm}^{-1}$  and  $611\text{ cm}^{-1}$  are observed, and can be attributed to the Co–O and Ni–O bond, respectively [37].

Raman spectroscopy is a sensitive and non-destructive technique, widely used to detect structural defects in systems containing  $\text{C sp}^2$ . The results obtained using this technique are shown in Figure S7. For both materials, peaks are observed at  $1574\text{ cm}^{-1}$  (G band) and another at  $1345\text{ cm}^{-1}$  (D band). The G band corresponds to the first-order scattering of the  $\text{E}_{2g}$  phonon, in the center of the Brillouin zone, and is typically associated with graphitic carbon structures [36,38]. The D band is attributed to the collective respiration modes of the rings within the graphene lattice, which may indicate a reduction in the size of the  $\text{C sp}^2$  domains via chemical oxidation of graphite [36,39]. The D band refers to amorphous carbon. The band at  $2699\text{ cm}^{-1}$  can also be observed, historically denominated the G' or 2D band. This band has nothing to do with the G peak, but is the second order of the zone boundary phonons [40]. According to López-Díaz et al. [41], the apparent band at  $2936\text{ cm}^{-1}$  corresponds to the D + D' band. This band corresponds to phonons with different moments, which for their activation, require structural defects caused by the change in the chemical structure of the material, caused by the oxidation of graphite.

According to the data obtained, it can be concluded that the synthesis of Ni/Co-GO NPs from spent Zn-C batteries was successful. This material was used in the catalysis of  $\text{NaBH}_4$  hydrolysis to produce hydrogen.

### 3.2. Hydrogen Evolution from $\text{NaBH}_4$

It is known that the production of hydrogen via hydrolysis of  $\text{NaBH}_4$  can be accelerated with the addition of inorganic or organic acids, but the rate of hydrolysis is better controlled by transition metals and their salts [42]. In general, doping the active components or supporting them on a porous substrate is also a viable way to increase the surface area of catalysts and reaction efficiency [43]. Nickel and cobalt metals were selected as catalysts for the hydrogen evolution reaction because they are low cost and do not present a risk of extinction. For this, different compositions involving an  $m(\text{Ni})/m(\text{Co})$  ratio were evaluated, and the results are shown in Figure 4.

It can be observed that the monometallic composition, i.e., Ni-GO NPs and Co-GO NPs, presented higher reaction speed, but with low efficiency, close to 50% for both materials. Probably, the hydrogen gas produced an agglomerate around the nanoparticle, preventing the decomposition of more borohydride in this saturated site. This phenomenon reduces the efficiency of reaction. On the other hand, bimetallic compositions showed better efficiency when compared to monometallic NPs, except for the composition of Ni/Co-GO NPs (50:50  $w/w$ ). These compositions also presented longer induction time, close to 35 s.

The induction time occurs as a moment of pre-catalysis of the reaction, in which a reactive species is formed to catalyze the reaction. Among the bimetallic compositions, the Ni/Co-GO NPs (60:40 *w/w*) showed better efficiency and speed, with a Hydrogen Generation Rate (HGR) of  $212.1 \text{ mL min}^{-1} \text{ g}^{-1}$  from borohydride consumed. This value is similar to the value reported by Liu et al. [20], who found a rate of  $228.5 \text{ mL min}^{-1} \text{ g}^{-1}$  using nickel–cobalt boride as a catalyst for the same reaction. Other works that used Ni- and Co-based catalysts for hydrogen evolution from  $\text{NaBH}_4$  hydrolysis are showed in Table 2, along with the material used in this work for comparison.

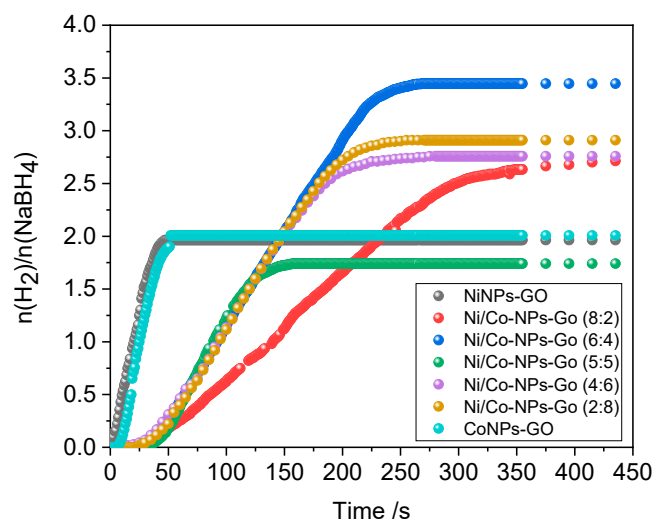


**Figure 4.** Hydrogen evolution from  $\text{NaBH}_4$  for different compositions of  $m(\text{Ni})/m(\text{Co})$  decorated in GO obtained from spent Zn-C batteries. Reaction conditions: GO support mass: 100 mg; 0.700 mmol of the catalyst; 1.00 mL of  $\text{NaBH}_4$  ( $0.500 \text{ mol L}^{-1}$ ); temperature: 296.15 K.

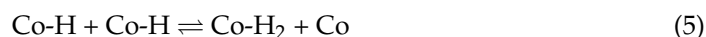
**Table 2.** Different Ni- and Co-based catalysts applied in the evolution of hydrogen from  $\text{NaBH}_4$ .

Catalyst	Hydrolysis Conditions	$E_a$ *	HGR **	Reference
Raney Ni–Co	0.5 g catalyst; 1 g $\text{NaBH}_4$ ; 10% wt NaOH; 293 K	52.3	228.5	[20]
Co-Ni $\theta$ C	50 mg catalyst; 0.1 g $\text{NaBH}_4$ ; 0.1 g NaOH; 298 K	30.3	6364	[22]
Ni-Co/r-GO	5 g of 10 wt% $\text{NaBH}_4$ ; 5 wt% NaOH; 0.05 g catalysts; 25 °C	55.12	1280	[23]
Ni-Co@3DG	0.02 g catalyst; 25 °C; 1 mol $\text{L}^{-1}$ $\text{NaBH}_4$ ; 20.0 mL NaOH; (pH = 10.0)	Not informed.	82.65	[24]
Co@C-650	10 mg of catalyst/5 mL $\text{H}_2\text{O}$ 2% m/m NaOH; 2% m/m $\text{NaBH}_4$ , 30 °C	41.5	330	[27]
Ni/Dolomita	5 mL de 0.25 mol $\text{L}^{-1}$ of NaOH; 60 °C; 100 mg $\text{NaBH}_4$ ; catalyst: 100 mg.	38.33	88.16	[44]
CoB-Ni $_4$ B $_3$	25 °C; 20 mg of catalyst; 10 mmol NaOH; 5 mL $\text{NaBH}_4$ 0.2 mol $\text{L}^{-1}$	32.7	404.6	[45]
Ni/Co-GO NPs	0.500 mol $\text{L}^{-1}$ $\text{NaBH}_4$ ; catalyst: 100 mg; 296.15 K; Without of NaOH	51.6	212.1	This work

\*  $E_a$  = Activation energy; \*\* HGR = Hydrogen Generation Rate.

Control assays were performed using GO without Ni and Co nanoparticles in the hydrogen evolution from borohydride. The material did not show considerable hydrogen formation. It can be concluded that the GO as a support for the nanoparticles favors the reaction kinetics.

$\text{NaBH}_4$  hydrolysis involves the dissociative chemisorption of  $\text{BH}_4^-$  on the catalyst surface as the first kinetic step. According to Guo et al. [46],  $\text{BH}_4^-$  ions are adsorbed on electron-enriched Co active sites, forming the  $\text{Co-BH}_3^-$  and  $\text{Co-H}$  intermediates, according to Equation (4).  $\text{Co-BH}_3^-$  reacts with water to form the intermediates  $\text{Co-H}$  and  $\text{BH}_3(\text{OH})^-$ . Two  $\text{Co-H}$  sites combine to form  $\text{H}_2$ , regenerating part of the active sites (Equation (5)).



The adsorption of  $\text{H}_2$  can block the active sites, decreasing the catalytic efficiency of the material. Thus, the bimetallic composition may allow the transport of  $\text{H}_2$  to Ni sites (Equations (6) and (7)), preventing the agglomeration and gas saturation on the surface of active Co sites, improving catalyst efficiency. Similar results were observed by Paksoy et al. [45], who used Bi-Ni-Co nanospheres in  $\text{NaBH}_4$  catalysis, and whose speed obtained was  $404.6 \text{ mL min}^{-1} \text{ g}^{-1}$ , for a composition 35/36% *w/w* Co-Ni.

### 3.3. Evaluation of the Influence of $\text{NaBH}_4$ Concentration

The evaluation of  $\text{NaBH}_4$  concentration in the evolution of hydrogen mediated by Ni/Co NPs-GO is shown in Figure 5a. It should be noted that the  $\text{H}_2/\text{NaBH}_4$  ratio is practically the same, regardless of the concentration of  $\text{NaBH}_4$  used. The kinetic constants were equal to  $4.2 \times 10^{-3} \text{ s}^{-1}$ ,  $3.1 \times 10^{-3} \text{ s}^{-1}$ ,  $3.2 \times 10^{-3} \text{ s}^{-1}$ , and  $3.6 \times 10^{-3} \text{ s}^{-1}$  for 0.2, 0.3, 0.4, and 0.5  $\text{mol L}^{-1}$ , respectively. The plot of the kinetic constant vs. the  $\ln$  of  $\text{NaBH}_4$  concentration is shown in Figure 5b, showing an almost horizontal line with a slope of  $-0.18$ . This suggests that the hydrolysis of  $\text{NaBH}_4$  catalyzed by Ni/Co-GO follows a zero-order reaction with respect to  $\text{NaBH}_4$  concentration. Consequently, this rules out  $\text{NaBH}_4$  activation as the sole rate-determining step. Similar results are discussed by Fu et al. [47].

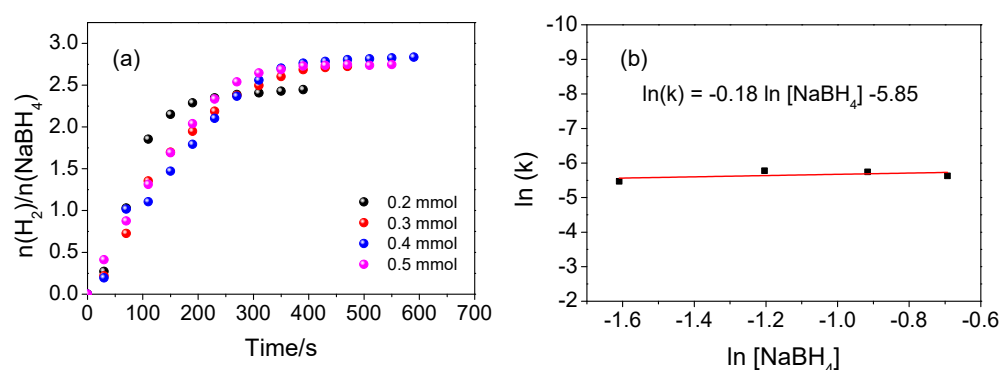


**Figure 5.** (a) Hydrogen evolution from different  $\text{NaBH}_4$  concentration. (b)  $\ln$  of kinetic constant vs. the  $\ln$  of  $\text{NaBH}_4$  concentration. Reaction conditions: 0.700 mmol of Ni/Co NPs (60:40 *w/w*); GO support: 100 mg; temperature: 296.15 K.

### 3.4. Evaluation of the Influence of Catalyst Dose

The evaluation of catalyst dose in the evolution of hydrogen mediated by Ni/Co NPs-GO is shown in Figure 6a. The catalyst dose increase from 0.175 mmol to 0.700 mmol increased the HGR from  $71.7 \text{ mL g}_{\text{cat}}^{-1} \text{ min}^{-1}$  to  $212.1 \text{ mL g}_{\text{cat}}^{-1} \text{ min}^{-1}$ . This result can be attributed to an increase in active sites, favoring the reaction kinetics.

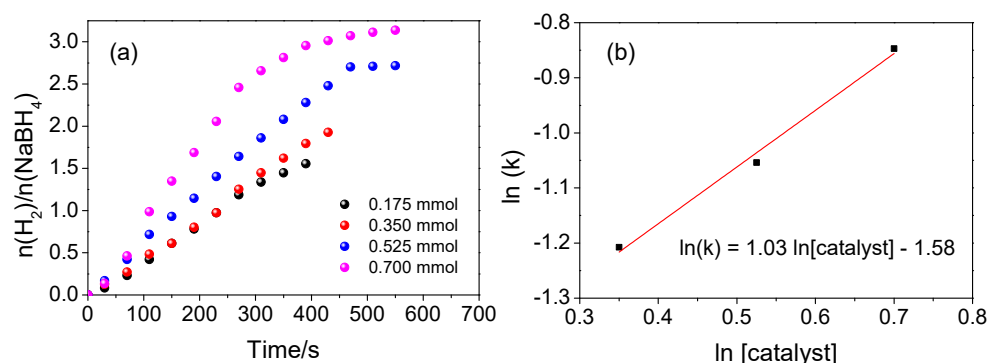


**Figure 6.** (a) Hydrogen evolution from  $\text{NaBH}_4$  for different doses of catalyst Ni/Co-GO NPs. (b)  $\ln$  of kinetic constant vs. the  $\ln$  of catalyst dose. Reaction conditions: 0.700 mmol of Ni/Co NPs (60:40  $w/w$ ); GO support: 100 mg; 1.00 mL of  $\text{NaBH}_4$  ( $0.500 \text{ mol L}^{-1}$ ); temperature: 296.15 K.

It is evident that the data for doses of 0.175 mmol and 0.350 mmol largely coincide. As a result, the data for 0.175 mmol were disregarded to create the plot of the kinetic constant versus the natural logarithm of catalyst dose (Figure 6b). The slope was 1.18, indicating a first-order kinetics with respect to the catalyst. Similar findings have been discussed by Fu et al. [47].

### 3.5. Evaluation of NaOH Presence in the Hydrogen Evolution

$\text{NaBH}_4$  is considered a very promising hydrogen storage. However, it presents low stability and a slow reaction rate in water in the absence of a catalyst. According to Schlesinger and coworkers [48], borohydride tends to stabilize in alkaline liquid solution, and therefore, this parameter is widely studied. The results of hydrogen evolution using Ni/Co-GO NPs (60:40  $w/w$ ) at different concentrations of NaOH are shown in Figure 7. As can be seen, the addition of NaOH decreases the yield. The increase in NaOH concentration from 0.010 to 0.05  $\text{mol L}^{-1}$  reduces the reaction yield from 71.4 to 8%, respectively. According to Guo et al. [46], the increase in sodium hydroxide concentration increases the concentration of  $\text{Na}^+$  ions. This is also due to the borohydride counterion being present in the solution. These ions can be deposited on the active sites of the catalyst, reducing the reaction rate and reaction yield. Thus, the other assays were performed without the addition of NaOH.

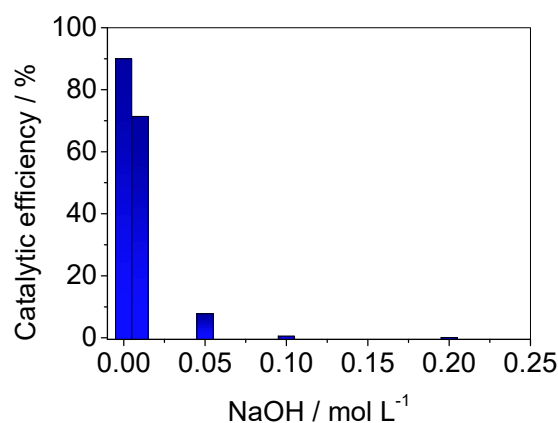


**Figure 7.** Catalytic efficiency of hydrogen evolution from  $\text{NaBH}_4$  in the presence of different concentrations of NaOH. Reaction conditions: 0.700 mmol of Ni/Co NPs (60:40  $w/w$ ), GO support: 100 mg; 1.00 mL of  $\text{NaBH}_4$  ( $0.500 \text{ mol L}^{-1}$ ); temperature: 296.15 K.

### 3.6. Evaluation of Temperature in the Hydrogen Evolution

The results of hydrogen evolution using the Ni/Co-GO NPs (60:40  $w/w$ ) at different temperatures are shown in Figure 8. The reaction rate is dependent of the temperature,

reaching higher kinetics at higher temperature values. The pseudo first-order kinetic models were fitted to the experimental data. The kinetic constants values ( $k_{\text{obs}}$ ) for each temperature are shown in the Table 3.

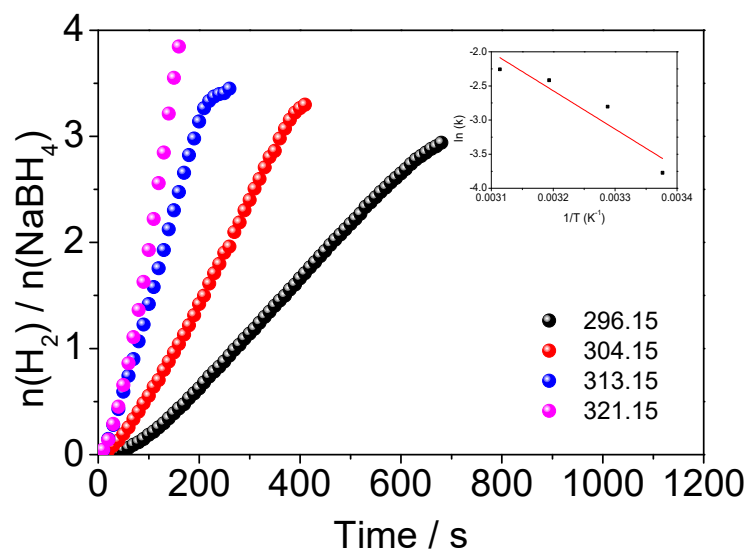


**Figure 8.** Hydrogen evolution from  $\text{NaBH}_4$  catalyzed with Ni/Co-GO NPs (60:40  $w/w$ ) in different temperatures. Reaction parameters: 0.700 mmol of Ni/Co-GO NPs (60:40  $w/w$ ), GO support: 100 mg; 1.00 mL of  $\text{NaBH}_4$  (0.500 mol  $\text{L}^{-1}$ ). Inset. Arrhenius plot ( $\ln k$  versus absolute temperature ratio). Data using 0.500 mol  $\text{L}^{-1}$   $\text{NaBH}_4$  solution and using NP-Ni/Co-GO (60:40  $w/w$ ) as flexible at different solution temperatures.

**Table 3.** Kinetic constants ( $k_{\text{obs}}$ ) of hydrogen evolution reaction from  $\text{NaBH}_4$  with Ni/Co-GO NPs (60:40  $w/w$ ) at different temperatures. Reaction parameters: 0.700 mmol of Ni/Co-GO NPs (60:40  $w/w$ ), GO support: 100 mg; 1.00 mL of  $\text{NaBH}_4$  (0.500 mol  $\text{L}^{-1}$ ); temperature: 296.15 K.

Temperature (Kelvin)	Reaction Kinetic Constant ( $\text{s}^{-1}$ )
296.15	0.0230
304.15	0.0606
313.15	0.0893
321.15	0.1047

From the kinetic constants, the Arrhenius graph was constructed (inset of Figure 6). The linear model was fitted to the experimental data, obtaining a coefficient of determination of 0.833. The activation energy of the system was determined according to Equation (2), which presented a value of 46.7  $\text{kJ mol}^{-1}$ . This result is consistent with the findings of Amendola et al. [49], who obtained a value of 47  $\text{kJ mol}^{-1}$ . The authors used a ruthenium-based catalyst for borohydride decomposition reactions to produce hydrogen gas. Paksoy et al. used the same metals, Co and Ni, supported with metal-boron crystals, which found an activation energy of 32.7  $\text{kJ mol}^{-1}$  [45]. Akbayrak et al. found an activation energy of 65  $\text{kJ mol}^{-1}$  using cobalt ferrite as a support for platinum nanoparticles [50]. The results indicate that it was possible to obtain a suitable material from spent Zn-C batteries for the efficient evolution of  $\text{H}_2$  from  $\text{NaBH}_4$ . From the obtained results, it was possible to determine the rate equation, according to Equation (8).

$$\text{Rate} = k [\text{NaBH}_4]^0 [\text{catalyst}]^1 \quad (8)$$

### 3.7. Reuse of the Material

The reuse of Ni/Co-GO NPs (60:40  $w/w$ ), which presented the better performance in hydrogen evolution from borohydride, was reused until it lost its efficiency. The results

are shown in Figure 9. There was a loss of efficiency (17%) between the first and second cycles, but it remained constant until the seventh cycle (70% yield). From the eighth cycle onwards, the efficiency decreases again, reaching an efficiency of 50% in the tenth cycle. Probably, the decline in efficiency from the eighth cycle onwards may be linked to catalyst leaching [51]. Comparable findings were noted by Khan et al., who detected catalyst leaching starting from the third cycle [52]. Efficiency in the reaction exhibited a decline over the course of three cycles when employing a Cu-based catalyst for hydrogen evolution in the methanolysis of  $\text{NaBH}_4$  [53]. Therefore, it can be concluded that the material is stable, as its performance remains satisfactory even after seven cycles of use.

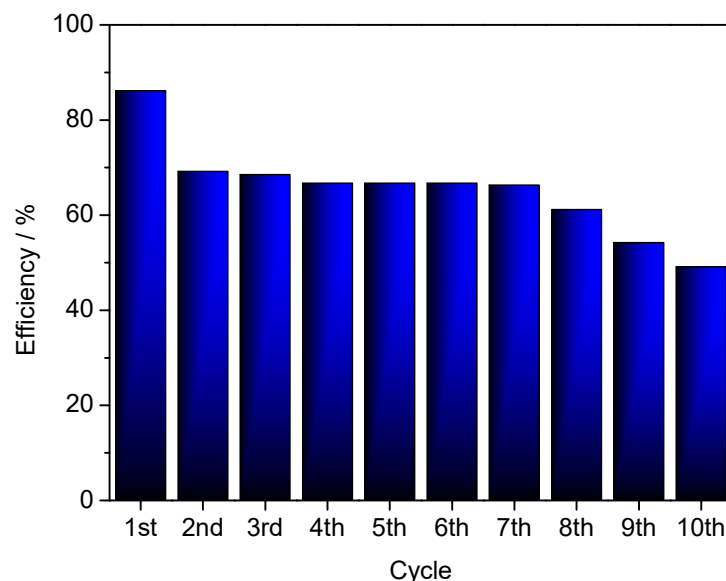


**Figure 9.** Reuse of Ni/Co-GO NPs (60:40 *w/w*) in hydrogen evolution from  $\text{NaBH}_4$ . Reaction parameters: 0.700 mmol of Ni/Co-GO NPs (60:40 *w/w*), GO support: 100 mg; 1.00 mL of  $\text{NaBH}_4$  ( $0.500 \text{ mol L}^{-1}$ ); temperature: 296.15 K.

### 3.8. Performance of Ni/Co Supported on GO Derived from Graphite in Zn-C Batteries and Analytical Grade

For comparative analysis, Ni/Co nanoparticles were deposited on analytical-grade Zn-C stack graphite-supported graphene oxide (GO). The results are shown in Figure S8. It is noticeable that the performance of both materials was quite similar, with a slightly higher yield for the material obtained from spent Zn-C batteries, while the kinetics were more favorable for the material derived from analytical-grade graphite. The commercial GO value is USD 0.045/g. Considering the inputs for producing GO from spent Zn-C batteries, the value reaches half. Considering the price and environmental appeal, the material obtained in this work appears to be competitive.

## 4. Conclusions

Based on the results achieved in this study, it can be asserted that a novel, value-added material was successfully obtained from graphite extracted from spent Zn-C batteries using an eco-friendly process. This approach offers a new method for treating and addressing waste that poses numerous environmental challenges, particularly in the context of urban mining. The synthesis of graphene oxide using the adapted Hummers method demonstrated characteristics comparable to those reported in the literature. Commercial graphene oxide is valued at USD 0.045/g, but when considering the inputs for producing graphene oxide from batteries, the cost is reduced by half. From both a cost and environmental perspective, the material obtained in this study appears to be competitive. When used as a support for metallic nanoparticles, this material exhibited promise in hydrogen evolution from sodium borohydride. It displayed kinetic constants in line with the literature, and the

rate of hydrogen generation was considered satisfactory. Notably, this study represents the first instance in the literature where graphene oxide obtained from e-waste is utilized as a support for metallic nanoparticles in hydrogen evolution. This aligns with the ongoing discourse surrounding alternative energy sources, opening new possibilities for hydrogen production from various sources. Furthermore, the material can be reused in multiple catalytic cycles, showcasing significant potential for applications in hydrogen evolution. Further studies are required to elucidate the reaction mechanism and explore the reasons behind the performance decline observed after the eighth cycle, as well as to explore other potential applications for graphene oxide support.

**Supplementary Materials:** The following supporting information can be downloaded at: <https://www.mdpi.com/article/10.3390/pr11113250/s1>, Figure S1: Hydrogen production reactor. Highlights: (a) Kitassato-type reactor; (b) rubber septum for sealing the system and injecting the NaBH<sub>4</sub> solution; (c) bath for temperature control; (d) magnetic stirrer with heating; (e) plastic hose connection between the reactor and the volume measurement system; (f) burette-type volume meter attached to the system to measure the volume of hydrogen gas produced; (g) water reservoir for water leveling in the volume measurement system; (h) digital thermometer; Figure S2: Graphene oxide produced from the rods of used Zn-C batteries; Figure S3: Transmission Electron Microscopy (TEM) image of graphene oxide (GO) obtained from spent Zn-C batteries. Inset: Selected-Area Electron Diffraction (SAED). Polycrystalline structure characterized by the main interplanar distances: 0.98 Å; 1.19 Å; 2.10 Å; 3.00 Å; Figure S4: Transmission Electron Microscopy image of Ni/Co-NPs-GO. Inset: Selected-Area Electron Diffraction (SAED). Polycrystalline structure characterized by the main interplanar distances: 1.22 Å; 1.65 Å; 2.06 Å; 3.19 Å; 3.80 Å; Figure S5: Energy Dispersive Spectroscopy (EDS). (A) Graphene oxide (GO) obtained from spent Zn-C batteries. (B) Ni/Co-NPs-GO (60:40 w/w); Figure S6: FTIR of (a) graphite obtained from spent Zn-C batteries (red) and graphene oxide (GO) obtained from spent Zn-C batteries (black) (b) Ni/Co-NPs-GO (60:40 w/w); Figure S7: Raman spectroscopy. (a) Graphite obtained from spent Zn-C batteries (b) graphene oxide (GO) obtained from spent Zn-C batteries; Figure S8: Hydrogen evolution from NaBH<sub>4</sub> mediated by Ni/Co-GO NPs. Reaction conditions: 0.700 mmol of Ni/Co NPs (60:40 w/w); GO support: 100 mg; 1.00 mL of NaBH<sub>4</sub> (0.500 mol L<sup>-1</sup>); temperature: 296.15 K.

**Author Contributions:** G.S.: conceptualization, methodology, investigation, formal analysis, writing—original draft, writing—review and editing; I.M.J.: conceptualization, methodology, investigation, formal analysis; E.B.: conceptualization, methodology, investigation; R.M.: conceptualization, methodology, resources, funding acquisition, investigation, formal analysis, writing—original draft, writing—review and editing, supervision. All authors have read and agreed to the published version of the manuscript.

**Funding:** This research received no external funding.

**Data Availability Statement:** Data sharing not applicable. No new data were created or analyzed in this study. Data sharing is not applicable to this article.

**Acknowledgments:** The authors thank the Coordenação de Aperfeiçoamento de Pessoal de Nível Superior—Brazil (CAPES), Conselho Nacional de Desenvolvimento Científico e Tecnológico (CNPq-Process: 405828/2022-5 and 312400/2021-7), Fundação de Amparo à Pesquisa do Estado de Minas Gerais (FAPEMIG, RED-00144-22), Department of Chemistry of Universidade Federal de Viçosa, Department of Physics of Universidade Federal de Viçosa, and the Center of Microscopy at the Universidade Federal de Minas Gerais (<http://www.microscopia.ufmg.br>, accessed on 10 September 2023, for providing the equipment and technical support for experiments involving electron microscopy.

**Conflicts of Interest:** The authors declare that they have no known competing financial interest or personal relationships that could have appeared to influence the work reported in this paper.

## References

1. Karthik, P.E.; Rajan, H.; Jothi, V.R.; Sang, B.I.; Yi, S.C. Electronic Wastes: A near Inexhaustible and an Unimaginably Wealthy Resource for Water Splitting Electrocatalysts. *J. Hazard. Mater.* **2022**, *421*, 126687. [PubMed]
2. Albright, G.; Edie AllCell Technologies, J.; Crossley, P.; Vassallo, A. *Battery Storage for Renewables: Market Status and Technology Outlook*; International Renewable Energy Agency: Masdar City, United Arab Emirates, 2015.

3. Bernardes, A.M.; Espinosa, D.C.R.; Tenório, J.A.S. Recycling of Batteries: A Review of Current Processes and Technologies. *J. Power Sources* **2004**, *130*, 291–298. [[CrossRef](#)]
4. Alcaraz, L.; García-Díaz, I.; González, L.; Rabanal, M.E.; Urbieto, A.; Fernández, P.; López, F.A. New Photocatalytic Materials Obtained from the Recycling of Alkaline and Zn/C Spent Batteries. *J. Mater. Res. Technol.* **2019**, *8*, 2809–2818. [[CrossRef](#)]
5. Vieira Segundo, J.E.D.; Vilar, E.O. Grafeno: Uma Revisão Sobre Propriedades, Mecanismos de Produção e Potenciais Aplicações Em Sistemas Energéticos. *Rev. Eletrônica De Mater. E Process.* **2016**, *11*, 54–57.
6. Yang, Q.; Cao, L.; Li, S.; Zeng, X.; Zhou, W.; Zhang, C. Upgrading Pomelo Peels into Laser-Induced Graphene for Multifunctional Sensors. *J. Anal. Appl. Pyrolysis* **2023**, *173*, 106074. [[CrossRef](#)]
7. Liu, Z.; Yang, Q.; Cao, L.; Li, S.; Zeng, X.; Zhou, W.; Zhang, C. Synthesis and Application of Porous Carbon Nanomaterials from Pomelo Peels: A Review. *Molecules* **2023**, *28*, 4429. [[CrossRef](#)] [[PubMed](#)]
8. Staudenmaier, L. Verfahren Zur Darstellung Der Graphitsäure. *Eur. J. Inorg. Chem.* **1898**, *31*, 1481–1487. [[CrossRef](#)]
9. Hofmann, U.; Rudorff, W. The Formation of Salts from Graphite by Strong Acids. *Trans. Faraday Soc.* **1938**, *45*, 1017–1021. [[CrossRef](#)]
10. Hummers, W.S.; Offeman, R.E. Preparation of Graphitic Oxide. *J. Am. Chem. Soc.* **1958**, *80*, 1339. [[CrossRef](#)]
11. Camargos, J.S.F.; Semmer, A.D.O.; Da Silva, S.N. Características e Aplicações do Grafeno e do Óxido de Grafeno e as Principais Rotas Para Síntese. *J. Eng. Exact Sci.* **2017**, *3*, 1118–1130. [[CrossRef](#)]
12. Loudiki, A.; Matrouf, M.; Azriouil, M.; Laghrib, F.; Farahi, A.; Bakasse, M.; Lahrach, S.; El Mhammedi, M.A. Graphene Oxide Synthesized from Zinc-Carbon Battery Waste Using a New Oxidation Process Assisted Sonication: Electrochemical Properties. *Mater. Chem. Phys.* **2022**, *275*, 125308. [[CrossRef](#)]
13. Joshi, D.J.; Koduru, J.R.; Malek, N.I.; Hussain, C.M.; Kailasa, S.K. Surface Modifications and Analytical Applications of Graphene Oxide: A Review. *TrAC-Trends Anal. Chem.* **2021**, *144*, 116448. [[CrossRef](#)]
14. Li, W.; Liu, Y.; Guo, F.; Du, Y.; Chen, Y. Self-Assembly Sandwich-like Fe, Co, or Ni Nanoparticles/Reduced Graphene Oxide Composites with Excellent Microwave Absorption Performance. *Appl. Surf. Sci.* **2021**, *562*, 150212. [[CrossRef](#)]
15. Dong, J.; Sun, T.; Zhang, Y.; Zhang, H.; Lu, S.; Hu, D.; Chen, J.; Xu, L. Mesoporous NiCo Alloy/Reduced Graphene Oxide Nanocomposites as Efficient Hydrogen Evolution Catalysts. *J. Colloid Interface Sci.* **2021**, *599*, 603–610. [[CrossRef](#)] [[PubMed](#)]
16. Grad, O.; Mihet, M.; Coros, M.; Dan, M.; Lazar, M.D.; Blanita, G. Reduced Graphene Oxide Modified with Noble Metal Nanoparticles for Formic Acid Dehydrogenation. *Catal. Today* **2021**, *366*, 41–47. [[CrossRef](#)]
17. Singla, S.; Sharma, S.; Basu, S.; Shetti, N.P.; Aminabhavi, T.M. Photocatalytic Water Splitting Hydrogen Production via Environmental Benign Carbon Based Nanomaterials. *Int. J. Hydrogen Energy* **2021**, *46*, 33696–33717. [[CrossRef](#)]
18. Jia, X.; Sang, Z.; Sun, L.; Xu, F.; Pan, H.; Zhang, C.; Cheng, R. Graphene-Modified Co-B-P Catalysts for Hydrogen Generation from Sodium Borohydride Hydrolysis. *Nanomaterials* **2022**, *12*, 2732. [[CrossRef](#)] [[PubMed](#)]
19. Rabia, M.; Hadia, N.M.A.; Farid, O.M.; Abdelazeez, A.A.A.; Mohamed, S.H.; Shaban, M. Poly(M-toluidine)/Rolled Graphene Oxide Nanocomposite Photocathode for Hydrogen Generation from Wastewater. *Int. J. Energy Res.* **2022**, *46*, 11943–11956. [[CrossRef](#)]
20. Liu, B.H.; Li, Z.P.; Suda, S. Nickel- and Cobalt-Based Catalysts for Hydrogen Generation by Hydrolysis of Borohydride. *J. Alloys Compd.* **2006**, *415*, 288–293. [[CrossRef](#)]
21. Darabdhara, G.; Amin, M.A.; Mersal, G.A.M.; Ahmed, E.M.; Das, M.R.; Zakaria, M.B.; Malgras, V.; Alshehri, S.M.; Yamauchi, Y.; Szunerits, S.; et al. Reduced Graphene Oxide Nanosheets Decorated with Au, Pd and Au-Pd Bimetallic Nanoparticles as Highly Efficient Catalysts for Electrochemical Hydrogen Generation. *J. Mater. Chem. A* **2015**, *3*, 20254–20266. [[CrossRef](#)]
22. Sun, L.; Gao, X.; Ning, X.; Qiu, Z.; Xing, L.; Yang, H.; Li, D.; Dou, J.; Meng, Y. Cobalt-Nickel Bimetal Carbon Sphere Catalysts for Efficient Hydrolysis of Sodium Borohydride: The Role of Synergy and Confine Effect. *Int. J. Hydrogen Energy* **2023**, *48*, 3413–3428. [[CrossRef](#)]
23. Chou, C.C.; Hsieh, C.H.; Chen, B.H. Hydrogen Generation from Catalytic Hydrolysis of Sodium Borohydride Using Bimetallic NiCo Nanoparticles on Reduced Graphene Oxide as Catalysts. *Energy* **2015**, *90*, 1973–1982. [[CrossRef](#)]
24. Karaman, O. Three-Dimensional Graphene Network Supported Nickel-Cobalt Bimetallic Alloy Nanocatalyst for Hydrogen Production by Hydrolysis of Sodium Borohydride and Developing of an Artificial Neural Network Modeling to Forecast Hydrogen Production Rate. *Chem. Eng. Res. Des.* **2022**, *181*, 321–330. [[CrossRef](#)]
25. Didehban, A.; Zabihi, M.; Babajani, N. Preparation of the Efficient Nano-Bimetallic Cobalt-Nickel Catalysts Supported on the Various Magnetic Substrates for Hydrogen Generation from Hydrolysis of Sodium Borohydride in Alkaline Solutions. *Polyhedron* **2020**, *180*, 114405. [[CrossRef](#)]
26. Yue, C.; Yang, P.; Wang, J.; Zhao, X.; Wang, Y.; Yang, L. Facile Synthesis and Characterization of Nano-Pd Loaded NiCo Microfibers as Stable Catalysts for Hydrogen Generation from Sodium Borohydride. *Chem. Phys. Lett.* **2020**, *743*, 137170. [[CrossRef](#)]
27. Su, S.; Chen, K.; Yang, X.; Dang, D. Coronavirus-like Core—Shell-Structured Co@C for Hydrogen Evolution via Hydrolysis of Sodium Borohydride. *Molecules* **2023**, *28*, 2–9. [[CrossRef](#)]
28. Zhao, W.; Kido, G.; Hara, K.; Noguchi, H. Characterization of Neutralized Graphite Oxide and Its Use in Electric Double Layer Capacitors. *J. Electroanal. Chem.* **2014**, *712*, 185–193. [[CrossRef](#)]
29. Zhang, D.; Cui, X.; Jin, G.; Jiao, Y.; Li, D. Preparation, Deposited Behavior and Hydrophobic Property of Modified Graphene Oxide Reinforced Ni Composite Coatings by Magnetic Field Assisted Electro-Brush Plating. *Surf. Coat. Technol.* **2020**, *403*, 126363. [[CrossRef](#)]

30. Stobinski, L.; Lesiak, B.; Malolepszy, A.; Mazurkiewicz, M.; Mierzwa, B.; Zemek, J.; Jiricek, P.; Bieloshapka, I. Graphene Oxide and Reduced Graphene Oxide Studied by the XRD, TEM and Electron Spectroscopy Methods. *J. Electron Spectrosc. Relat. Phenom.* **2014**, *195*, 145–154. [[CrossRef](#)]
31. Saxena, S.; Tyson, T.A.; Shukla, S.; Negusse, E.; Chen, H.; Bai, J. Investigation of Structural and Electronic Properties of Graphene Oxide. *Appl. Phys. Lett.* **2011**, *99*, 5–8. [[CrossRef](#)]
32. Aliyev, E.; Filiz, V.; Khan, M.M.; Lee, Y.J.; Abetz, C.; Abetz, V. Structural Characterization of Graphene Oxide: Surface Functional Groups and Fractionated Oxidative Debris. *Nanomaterials* **2019**, *9*, 1180. [[CrossRef](#)] [[PubMed](#)]
33. Jacob, B.; Mohan, M.; Dhanyaprabha, K.C.; Thomas, H. NiCo<sub>2</sub>O<sub>4</sub> Nanoparticles Anchored on Reduced Graphene Oxide with Enhanced Catalytic Activity towards the Reduction of P-Nitrophenol in Water. *Colloids Surf. A Physicochem. Eng. Asp.* **2022**, *643*, 128717. [[CrossRef](#)]
34. Xu, H.; Shi, Z.X.; Tong, Y.X.; Li, G.R. Porous Microrod Arrays Constructed by Carbon-Confined NiCo@NiCoO<sub>2</sub> Core@Shell Nanoparticles as Efficient Electrocatalysts for Oxygen Evolution. *Adv. Mater.* **2018**, *30*, e1705442. [[CrossRef](#)] [[PubMed](#)]
35. Shi, C.; Cao, H.; Li, S.; Guo, L.; Wang, Y.; Yang, J. Flexible Nickel Cobalt Metal-Organic Frameworks/Reduced Graphene Oxide Hybrid Film for High-Performance Supercapacitors. *J. Energy Storage* **2022**, *54*, 105270. [[CrossRef](#)]
36. Rattana, T.; Chaiyakun, S.; Witit-Anun, N.; Nuntawong, N.; Chindaudom, P.; Oaew, S.; Kedkeaw, C.; Limsuwan, P. Preparation and Characterization of Graphene Oxide Nanosheets. *Procedia Eng.* **2012**, *32*, 759–764. [[CrossRef](#)]
37. Naveen, A.N.; Selladurai, S. Novel Low Temperature Synthesis and Electrochemical Characterization of Mesoporous Nickel Cobaltite-Reduced Graphene Oxide (RGO) Composite for Supercapacitor Application. *Electrochim. Acta* **2015**, *173*, 290–301. [[CrossRef](#)]
38. Caridad, J.M.; Rossella, F.; Bellani, V.; Grandi, M.S.; Diez, E. Automated Detection and Characterization of Graphene and Few-Layer Graphite via Raman Spectroscopy. *J. Raman Spectrosc.* **2011**, *42*, 286–293. [[CrossRef](#)]
39. Gao, J.; Liu, F.; Liu, Y.; Ma, N.; Wang, Z.; Zhang, X. Environment-Friendly Method to Produce Graphene That Employs Vitamin C and Amino Acid. *Chem. Mater.* **2010**, *22*, 2213–2218. [[CrossRef](#)]
40. Ferrari, A.C.; Meyer, J.C.; Scardaci, V.; Casiraghi, C.; Lazzeri, M.; Mauri, F.; Piscanec, S.; Jiang, D.; Novoselov, K.S.; Roth, S.; et al. Raman Spectrum of Graphene and Graphene Layers. *Phys. Rev. Lett.* **2006**, *97*, 187401. [[CrossRef](#)]
41. López-Díaz, D.; López Holgado, M.; García-Fierro, J.L.; Velázquez, M.M. Evolution of the Raman Spectrum with the Chemical Composition of Graphene Oxide. *J. Phys. Chem. C* **2017**, *121*, 20489–20497. [[CrossRef](#)]
42. Liu, Y.; Yang, Y.; Gao, M.; Pan, H. Tailoring Thermodynamics and Kinetics for Hydrogen Storage in Complex Hydrides towards Applications. *Chem. Rec.* **2016**, *16*, 189–204. [[CrossRef](#)]
43. Zou, Y.; Yin, Y.; Gao, Y.; Xiang, C.; Chu, H.; Qiu, S.; Yan, E.; Xu, F.; Sun, L. Chitosan-Mediated Co–Ce–B Nanoparticles for Catalyzing the Hydrolysis of Sodium Borohydride. *Int. J. Hydrogen Energy* **2018**, *43*, 4912–4921. [[CrossRef](#)]
44. Kiren, B.; Ayas, N. Nickel Modified Dolomite in the Hydrogen Generation from Sodium Borohydride Hydrolysis. *Int. J. Hydrogen Energy* **2021**, *47*, 19702–19717. [[CrossRef](#)]
45. Paksoy, A.; Kurtoglu, S.F.; Dizaji, A.K.; Altıntaş, Z.; Khoshsima, S.; Uzun, A.; Balci, Ö. Nanocrystalline Cobalt–Nickel–Boron (Metal Boride) Catalysts for Efficient Hydrogen Production from the Hydrolysis of Sodium Borohydride. *Int. J. Hydrogen Energy* **2021**, *46*, 7974–7988. [[CrossRef](#)]
46. Guo, J.; Hou, Y.; Li, B.; Liu, Y. Novel Ni–Co–B Hollow Nanospheres Promote Hydrogen Generation from the Hydrolysis of Sodium Borohydride. *Int. J. Hydrogen Energy* **2018**, *43*, 15245–15254. [[CrossRef](#)]
47. Fu, F.; Wang, C.; Wang, Q.; Martinez-Villacorta, A.M.; Escobar, A.; Chong, H.; Wang, X.; Moya, S.; Salmon, L.; Fouquet, E.; et al. Highly Selective and Sharp Volcano-Type Synergistic Ni<sub>2</sub>Pt@ZIF-8-Catalyzed Hydrogen Evolution from Ammonia Borane Hydrolysis. *J. Am. Chem. Soc.* **2018**, *140*, 10034–10042. [[CrossRef](#)] [[PubMed](#)]
48. Schlesinger, H.I.; Brown, H.C.; Finholt, A.E.; Gilbreath, J.R.; Hoekstra, H.R.; Hyde, E.K. Sodium Borohydride, Its Hydrolysis and Its Use as a Reducing Agent and in the Generation of Hydrogen. *J. Am. Chem. Soc.* **1953**, *75*, 215–219. [[CrossRef](#)]
49. Amendola, S.C.; Sharp-Goldman, S.L.; Saleem Janjua, M.; Kelly, M.T.; Petillo, P.J.; Binder, M. An Ultrasafe Hydrogen Generator: Aqueous, Alkaline Borohydride Solutions and Ru Catalyst. *J. Power Sources* **2000**, *85*, 186–189. [[CrossRef](#)]
50. Akbayrak, S.; Özkaz, S. Cobalt Ferrite Supported Platinum Nanoparticles: Superb Catalytic Activity and Outstanding Reusability in Hydrogen Generation from the Hydrolysis of Ammonia Borane. *J. Colloid Interface Sci.* **2021**, *596*, 100–107. [[CrossRef](#)]
51. Xu, D.; Zhang, Y.; Guo, Q. Research Progress on Catalysts for Hydrogen Generation through Sodium Borohydride Alcoholysis. *Int. J. Hydrogen Energy* **2022**, *47*, 5929–5946. [[CrossRef](#)]
52. Khan, S.B.; Ali, F.; Asiri, A.M. Metal Nanoparticles Supported on Polyacrylamide Water Beads as Catalyst for Efficient Generation of H<sub>2</sub> from NaBH<sub>4</sub> Methanolysis. *Int. J. Hydrogen Energy* **2020**, *45*, 1532–1540. [[CrossRef](#)]
53. Khan, S.B. Metal Nanoparticles Containing Chitosan Wrapped Cellulose Nanocomposites for Catalytic Hydrogen Production and Reduction of Environmental Pollutants. *Carbohydr. Polym.* **2020**, *242*, 116286. [[CrossRef](#)] [[PubMed](#)]

**Disclaimer/Publisher’s Note:** The statements, opinions and data contained in all publications are solely those of the individual author(s) and contributor(s) and not of MDPI and/or the editor(s). MDPI and/or the editor(s) disclaim responsibility for any injury to people or property resulting from any ideas, methods, instructions or products referred to in the content.